Title
Quantum interference mediated vertical molecular tunneling transistors.

Journal
Science advances, 4(10)

ISSN
2375-2548

Authors
Jia, Chuancheng
Famili, Marjan
Carlotti, Marco
et al.

Publication Date
2018-10-01

DOI
10.1126/sciadv.aat8237

Peer reviewed

APPLIED PHYSICS

Quantum interference mediated vertical molecular tunneling transistors

Chuancheng Jia[1]*, Marjan Famili[2]*, Marco Carlotti[3], Yuan Liu[4,5], Peiqi Wang[1,4], Iain M. Grace[2], Ziying Feng[1], Yiliu Wang[1], Zipeng Zhao[4], Mengning Ding[4], Xiang Xu[1], Chen Wang[4], Sung-Joon Lee[4], Yu Huang[4,6], Ryan C. Chiechi[3], Colin J. Lambert[2†], Xiangfeng Duan[1,6†]

Molecular transistors operating in the quantum tunneling regime represent potential electronic building blocks for future integrated circuits. However, due to their complex fabrication processes and poor stability, traditional molecular transistors can only operate stably at cryogenic temperatures. Here, through a combined experimental and theoretical investigation, we demonstrate a new design of vertical molecular tunneling transistors, with stable switching operations up to room temperature, formed from cross-plane graphene/self-assembled monolayer (SAM)/gold heterostructures. We show that vertical molecular junctions formed from pseudo-*p*-bis((4-(acetylthio)phenyl)ethynyl)-*p*-[2,2]cyclophane (PCP) SAMs exhibit destructive quantum interference (QI) effects, which are absent in 1,4-bis(((4-acetylthio)phenyl)ethynyl)benzene (OPE3) SAMs. Consequently, the zero-bias differential conductance of the former is only about 2% of the latter, resulting in an enhanced on-off current ratio for (PCP) SAMs. Field-effect control is achieved using an ionic liquid gate, whose strong vertical electric field penetrates through the graphene layer and tunes the energy levels of the SAMs. The resulting on-off current ratio achieved in PCP SAMs can reach up to ~330, about one order of magnitude higher than that of OPE3 SAMs. The demonstration of molecular junctions with combined QI effect and gate tunability represents a critical step toward functional devices in future molecular-scale electronics.

INTRODUCTION

Molecular electronics represent an attractive alternative for future electronic devices with rich functionalities beyond current scaling limits (*1*, *2*). Since molecular electronic devices can operate in the quantum tunneling regime, even at room temperature, numerous quantum phenomena at the subnanometer scale, such as nuclear spin resonance (*3*), quantum plasmons (*4*), thermoelectric effects (*5*), and quantum interference (QI) effects (*6*, *7*), can be explored. Furthermore, with properly designed device structures and functional molecules (*8*), various functions can be implemented in molecular tunneling junctions, such as switches (*9*–*11*), diodes (*12*, *13*), and transistors (*14*, *15*). Normally, molecular tunneling transistors, which are the most probable electronic element in future integrated circuits, are fabricated by placing a solid back gate (*16*) or electrochemical gate (*17*) to the side of molecular junctions to tune the energy levels of the central molecules. However, due to the complex device fabrication processes and low stability of these devices, these molecular transistors can typically only operate stably at cryogenic temperatures.

Here, we report a novel design of a vertical molecular tunneling transistor with stable operation up to room temperature based on a gate/graphene/self-assembled monolayer (SAM)/gold cross-plane vertical heterostructure (*18*, *19*). The conformation and binding geometry of the molecules in the SAM are fixed (*20*) by thiol anchor groups to the gold electrode, which ensures stable charge transport across the molecular junctions. A strong gating electric field, generated from the electrical double layer (EDL) of ionic liquid (*21*), is vertically applied to the graphene/SAM/gold junctions. Because of the partial electrostatic transparency of graphene (*22*), the applied electric field penetrates through the graphene layer and tunes the energy levels of the SAM relative to the Dirac point of the graphene, resulting in effective gate control and a significant conductance modulation in the molecular transistors. By exploiting the molecules with destructive QI effect to suppress the molecular conductance at low bias (*6*), we demonstrate molecular transistors with greatly improved on-off current ratio compared to those without destructive QI effects (*23*).

RESULTS AND DISCUSSION

Construction of the transistors

The vertical molecular tunneling transistors are shown schematically in Fig. 1A (see Materials and methods and fig. S1 for detailed fabrication process). Specifically, an ultraflat Au film is deposited on the exposed conducting silicon surface in a small hole at the center of a silicon/SiO_2 chip, which is connected to a metal electrode at the corner and used as the source electrode. An SAM of pseudo-*p*-bis((4-(acetylthio)phenyl)ethynyl)-*p*-[2,2]cyclophane (PCP) or 1,4-bis(((4-acetylthio)phenyl)ethynyl)benzene (OPE3) molecules (Fig. 1, B and C) is then functionalized on the Au film and confirmed by atomic force microscopy (AFM), Raman characterization, and x-ray photoelectron spectroscopy (XPS) (figs. S2 and S3). A chemical vapor deposition (CVD)–grown single-layer graphene (SLG) (fig. S2D) is then transferred and patterned on the top of corresponding SAMs. A drain electrode connecting with the graphene sheet and gate electrode is laid around the functional center. Last, the graphene/SAM/gold channel and gate electrode are covered by a small amount of diethylmethyl(2-methoxyethyl)ammonium bis(trifluoromethylsulfonyl)imide (DEME-TFSI) ionic liquid. Since the conformation and binding geometry of the molecules are fixed in SAMs (*20*) and the encapsulation by graphene electrodes prevents direct contact with ionic liquid, stable devices with low-noise operation can be realized.

[1]Department of Chemistry and Biochemistry, University of California, Los Angeles, Los Angeles, CA 90095, USA. [2]Physics Department, Lancaster University, Lancaster LA1 4YB, UK. [3]Stratingh Institute for Chemistry and Zernike Institute for Advanced Materials, University of Groningen, Nijenborgh 4, Groningen 9747 AG, Netherlands. [4]Department of Materials Science and Engineering, University of California, Los Angeles, Los Angeles, CA 90095, USA. [5]Key Laboratory for Micro-Nano Optoelectronic Devices of Ministry of Education, School of Physics and Electronics, Hunan University, Changsha 410082, China. [6]California NanoSystems Institute, University of California, Los Angeles, Los Angeles, CA 90095, USA.
*These authors contributed equally to this work.
†Corresponding author. Email: xduan@chem.ucla.edu (X.D.); c.lambert@lancaster.ac.uk (C.J.L.)

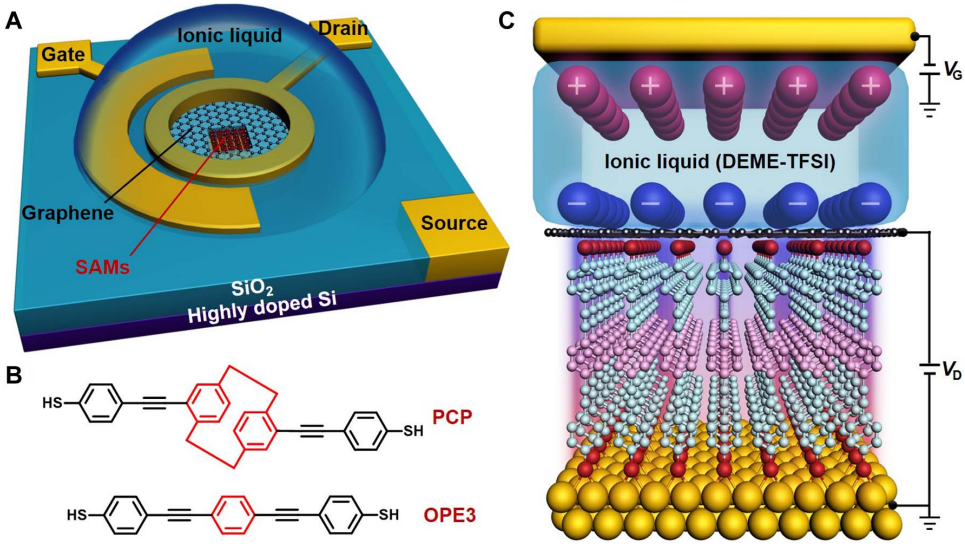

Fig. 1. Schematic illustration of the vertical molecular tunneling transistor. (**A**) Schematic illustration of the overall device structure. (**B**) Chemical structure of the PCP and OPE3 molecules. (**C**) Schematic illustration of the molecular transistor with OPE3 SAMs and ionic liquid (DEME-TFSI) gating. $DEME^+$ ions are the cations, and $TFSI^-$ ions comprise the anions.

Charge transport in molecular junctions

In contrast to the fully conjugated molecular chain in OPE3, a fundamental difference of PCP molecules is the presence of spatially separated aromatic rings linked by saturated methylene bridges in PCP. In this case, a current path mediated by π-π overlap between aromatic rings acts in parallel with current paths through the methylene bridges to create destructive QI features between the highest occupied molecular orbital (HOMO) and the HOMO-1, as shown in fig. S4 (A and B) and in the literature (*23*). When combined with interruption of the conjugation in the PCP molecule, this results in a lower transmission coefficient $T(E)$ for the PCP molecule compared with OPE3. As shown in Fig. 2B, the computed ratio of their transmission coefficients in graphene-molecule gold junctions for PCP and OPE at $E = E_F^{Gold}$ (where E_F^{Gold} is the Fermi energy of the gold electrode) is $\frac{T_{OPE}(E_F^{Gold})}{T_{PCP}(E_F^{Gold})} \approx 135$.

To fully understand the origin of this difference, a comparison between the molecular orbitals of PCP and OPE3 is presented in fig. S4C (*24*), along with a discussion of their mutual QI features.

The experimental current density (J_D) versus bias voltage V_D and the differential conductance (dJ/dV) versus V_D are shown in Fig. 2 (C and D). The current density (J_D) for the PCP junction is considerably lower than that of the OPE3 junction, especially near zero bias, which is consistent with the transmission coefficient characteristics of the respective molecules discussed above. The minima in the dJ/dV curves are associated with the Dirac point of the graphene, and their positions relative to the zero V_D indicate whether the graphene is p-doped or n-doped. In Fig. 2D, the Dirac point for OPE3 and PCP samples occurs at −0.3 and 0 V, respectively, indicating that the graphene is n-doped in the OPE3 sample and negligibly doped in PCP sample. For this reason, in what follows, when comparing our calculated $T(E)$ with experiments, the band structure of the graphene is adjusted to place the Dirac point of the OPE3 system at −0.3 eV and of the PCP system at 0 eV.

Figure 3 (D and G) shows the V_D dependence of $T(E)$ versus $E - E_F^{Gold}$ for PCP and OPE3. It is assumed that the energies of the molecular levels relative to E_F^{Gold} are independent of V_D and that positive (negative) bias voltage decreases (increases) the Dirac point relative to E_F^{Gold} (Eq. 1 in the "Theoretical methods" section). The current is computed using Eq. 4 (see the "Theoretical methods" section) by evaluating individual transmission coefficients $T(E, V_D, V_G)$ at every V_D value and computing the associated current. The dI/dV curves are then obtained by differentiating the current with respect to V_D.

From the experimental results of Fig. 2D, the value of dJ/dV at zero bias for OPE3 is 71 times larger than that for PCP. From statistics of 12 different experimental PCP and OPE3 junctions, the zero-bias differential conductance for OPE3 is 56 times larger than that for PCP (section S4). This ratio is comparable with the value of 65 obtained from the calculated results of Fig. 2F. For PCP and OPE3 junctions with gold-molecule-gold contacts (fig. S4, A and B), the conductance ratio at zero bias is $G_{OPE3}/G_{PCP} = 5$, which is only about one-tenth of junctions with gold-molecule-graphene contacts. This indicates that the conductance for molecule junctions with graphene electrode is more sensitive to the structure of molecules and their relative energy alignment.

Field effect properties of the transistors

To probe the field effect transistor functions of the molecular junctions, DEME-TFSI ionic liquid was used for gating, which has a high ionic conductivity, a large electrochemical window, and a low glass transition temperature of 182 K for ion migration (*25*). When a gate voltage (V_G) is applied to the gate electrode, a Helmholtz EDL is expected to self-organize on the surface of graphene/SAM/gold junction (Fig. 3A) with generation of a strong electric field of up to ~10 MV/cm (*21*). The gate performances for PCP and OPE3 transistors were measured at both room temperature (298 K) and 200 K and show similar characteristics between the two temperatures (Fig. 4 and fig. S7, A to L). Figure 4 (A and D) shows typical gate-dependent J_D-V_D characteristics measured at 200 K for PCP and OPE3. With V_G changing from −1 to 1 V, J_D greatly increases with V_G for negative V_D, while J_D greatly decreases with V_G for positive V_D. On the other hand, the gate-dependent J_D amplitude for OPE3 is evidently much smaller than that for PCP. This demonstrates the better gate control over the vertical PCP molecular transistors compared with OPE3.

The conductance minima for both molecules move in a positive (negative) direction along the V_D axis when the V_G is increased

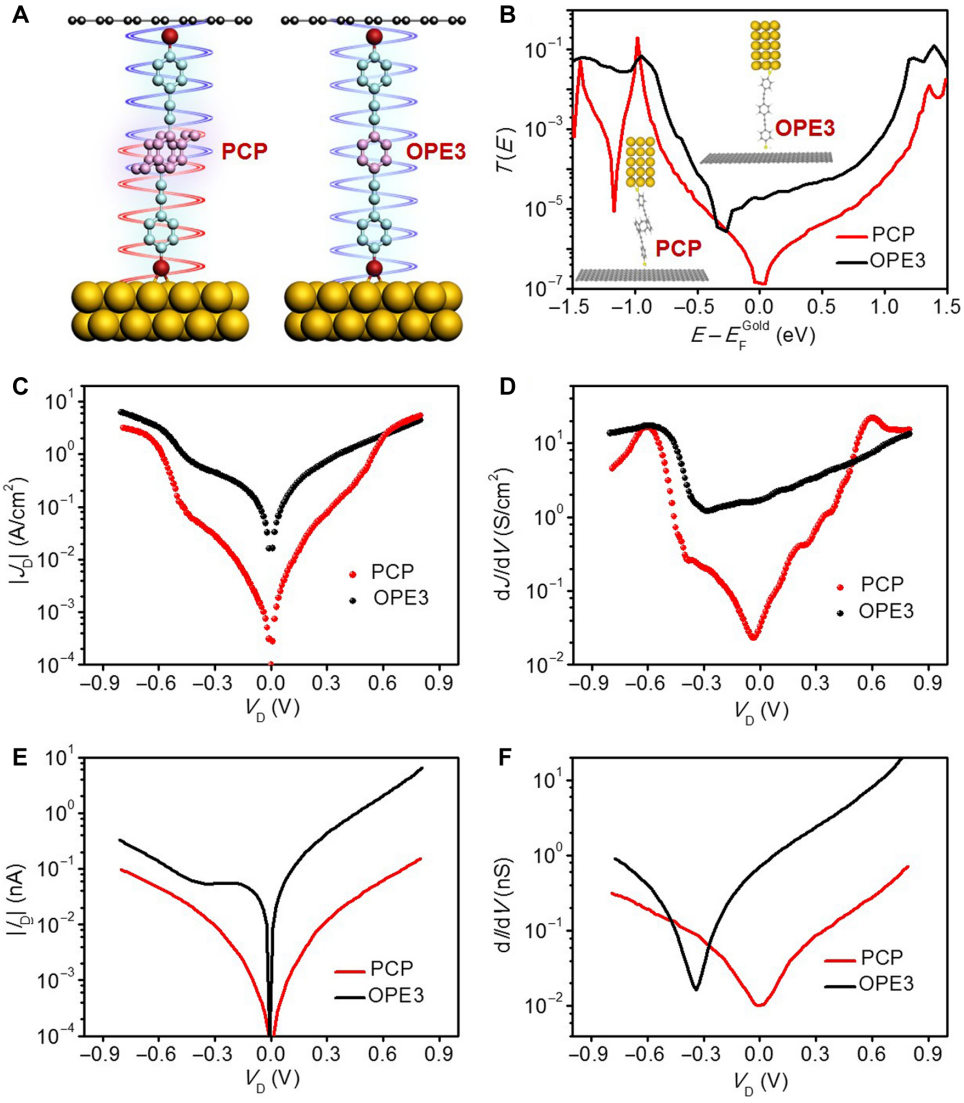

Fig. 2. Charge transport in molecular junctions. (**A**) Schematic illustration of the PCP and OPE3 junctions. (**B**) Transmission functions $T(E)$ for PCP (red) and OPE3 (black). Insets show the junction structures for simulation. (**C**) Plots of experimental current density (J_D) versus bias voltage (V_D) for PCP and OPE3. (**D**) Experimental differential conductance (dJ/dV) versus V_D plots for PCP and OPE3. (**E**) Theoretical current (I_D) versus V_D plots for PCP and OPE3. (**F**) Theoretical differential conductance (dI/dV) versus V_D plots for PCP and OPE3.

(decreased) (Fig. 4, B and E). This feature is independent of the type of molecule and is a reflection of the V_G dependence of the Dirac point of graphene (Fig. 3B). Figure 4C shows a two-dimensional visualization of dJ/dV plotted versus V_G and V_D for PCP. The oblique diamond-shaped low-conductance region (green) indicates off-resonant transport, while the red-orange high-conductance region outside the diamond is due to the conductive frontier molecular orbitals entering the bias window. Furthermore, a blue minimum conductance region appears at the center of the diamond, which corresponds to the Dirac point of the graphene. For the OPE3 transistor (Fig. 4F), a similar oblique diamond-shaped low-conductance region can be observed as well. However, the relative conductance changing between center low and outside high-conductance regions for OPE3 is considerably smaller than that for PCP, which reflects the better gating tunability for PCP. This is in agreement with the calculated $T(E)$ for PCP and OPE3 (Fig. 2B), as the difference between off-resonant and resonant transport is more pronounced for PCP in comparison with OPE3. Furthermore, the V_G/V_D slope for the edges of diamonds at the second and fourth quadrants is 0.2095 for OPE3, which is smaller than that for PCP with a value of 0.2493. This further demonstrates that the gate controllability for PCP is better than that for OPE3.

Working mechanism of the transistors

Figure 3C illustrates how the V_G induced by the ionic liquid affects the band structure of the graphene and the molecular energy levels. Note that the Fermi energy (E_F^{Gold}) of the gold is independent of V_G or V_D, since it is earthed in this study. In our theoretical model, the V_G can move the energy levels of the graphene, as well as molecular energy levels (Eqs. 1, 2, and 3 in the "Theoretical methods" section). Therefore, the position of the highest occupied molecular orbital (HOMO) and lowest unoccupied molecular orbital (LUMO) relative to the Fermi energy of the gold varies with V_G.

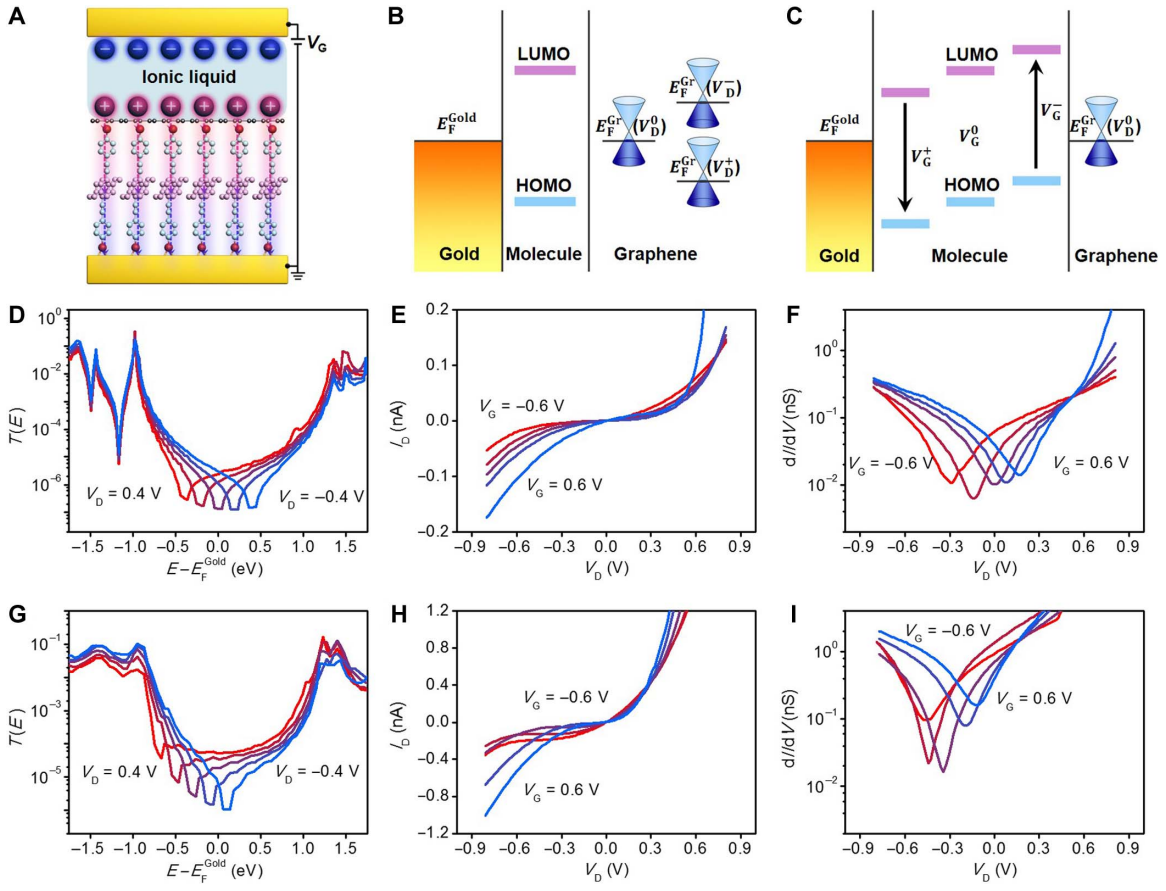

Fig. 3. Charge transport in vertical molecular transistors. (**A**) Schematic illustration of the working device with EDLs. (**B**) Schematic band diagram of the device with changed V_D at graphene electrode. (**C**) Schematic band diagram of the device with changed V_G. (**D** and **G**) Transmission coefficient $T(E)$ versus $E - E_F^{Gold}$ for PCP (D) and OPE3 (G) junctions for $-0.4 < V_D < 0.4$ with steps of 0.2 V. (**E** and **H**) Gate-dependent theoretical I_D-V_D characteristics for PCP (E) and OPE3 (H). (**F** and **I**) Gate-dependent theoretical dI/dV-V_D for PCP (F) and OPE3 (I). V_G is varied from −0.6, −0.3, 0.0, 0.3, to 0.6 V in (E), (F), (H), and (I).

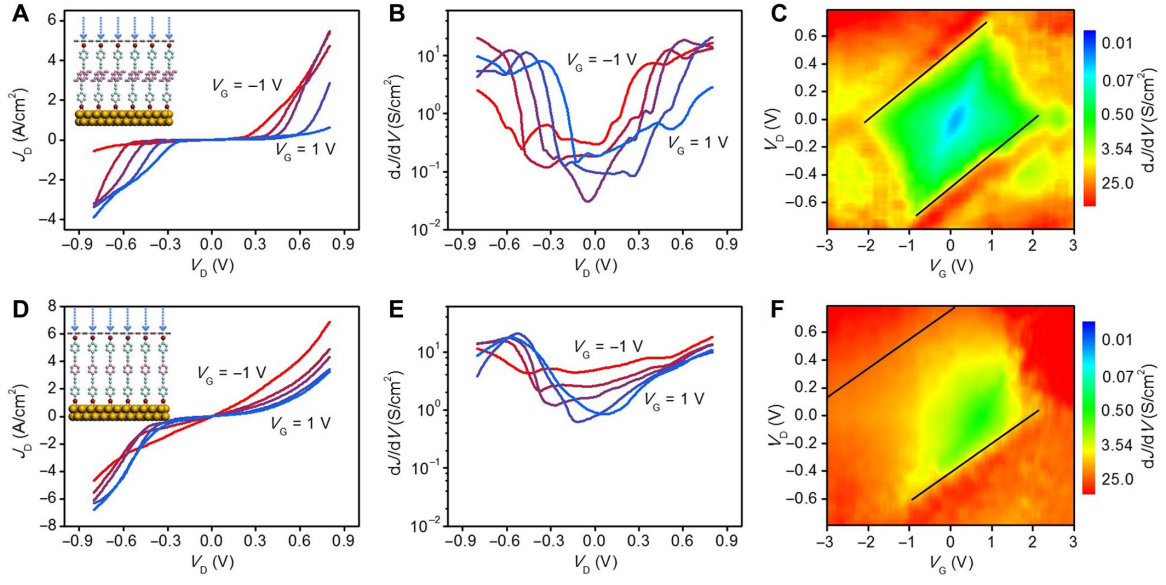

Fig. 4. Gating charge transport in experimental molecular transistors. (**A** and **B**) J_D versus V_D characteristics (A) and dJ/dV versus V_D characteristics (B) for PCP with V_G varying from −1 to 1 V with step of 0.5 V. (**C**) Two-dimensional visualization of dJ/dV plotted versus V_G and V_D for PCP. (**D** and **E**) J_D-V_D characteristics (D) and dJ/dV-V_D characteristics (E) for OPE3 with gating from −1 to 1 V with step of 0.5 V. (**F**) Two-dimensional visualization of dJ/dV plotted versus V_G and V_D for OPE3. Insets in (A) and (D) show schematics of the PCP and OPE3 transistors with applied vertical electric field. Black lines in (C) and (F) are auxiliary markers of corresponding conductance diamond edge.

Similar to the bias voltage lever arm (α), we consider a V_G lever arm (β in Eq. 1; see the "Theoretical methods" section). In the experimental dJ/dV of the OPE3 sample, we can see that the Dirac point of graphene moves up by 0.4 V when the V_G is increased by 1 V (Fig. 4E). For a similar change in V_G, the Dirac point moves up by 0.5 V in the PCP sample (Fig. 4B). Therefore, to compare our calculations with experiment, we choose β = 0.4. This assumption allows us to model the sensitivity of these devices to the change in V_G and V_D and yields agreement with our experiments. For example, a 1.2-V change in the V_G of the PCP device moves the Dirac point of the graphene by 0.48 V along the V_D axis (red curve and blue curve in Fig. 3F). Similar behavior also occurs in OPE3 junctions (Fig. 3I), namely, the orbital energies only vary with V_G, whereas the Dirac point and transmission minima are sensitive to both V_D and V_G (Fig. 3C).

The V_D- and V_G-dependent transmission coefficient $T(E, V_D, V_G)$ was calculated using a quantum transport code, the GOLLUM (*26*), and the current obtained from Eq. 4 (see the "Theoretical methods"). The theoretical gate-dependent I_D-V_D characteristics for PCP (Fig. 3E) reveal that, when V_G changes from −0.6 to 0.6 V, I_D greatly increases with V_G for negative V_D, while I_D decreases with V_G for positive V_D. A similar theoretical gate-dependent I_D-V_D characteristic is also obtained for OPE3 (Fig. 3H), although the gate-dependent change in I_D is smaller than that for PCP. Furthermore, from the gate-dependent dI/dV-V_D characteristics for PCP (Fig. 3F), it can be observed that the dI/dV-V_D curve shifts in a positive direction with V_G changing from −0.6 to 0.6 V, especially for the lowest conductance points. For OPE3, a similar gate-dependent dI/dV-V_D curve is obtained, but with a relatively smaller amplitude (Fig. 3I), in qualitative agreement with the experimental results (Fig. 4).

Transfer characteristics of the transistors

Transfer characteristics, which monitor the current modulation by varying V_G at a fixed V_D, are widely used for evaluating the performance of transistors (*27*). Experimental transfer characteristics (J_D-V_G) for PCP at V_D = −0.1, −0.2, −0.4, −0.6, and −0.8 V are shown in Fig. 5A. It can be observed that the lowest current point at V_D = −0.1 V is near V_G = 0 V, and as V_D increases from −0.1 to −0.8 V, the lowest current point shifts to a more negative V_D. This shifting of the lowest current point is due to variation on the Dirac point of the graphene electrode. With a more negative V_D, an increased negative V_G is needed to move the central transmission dip of the junction to the middle of the bias window. Similar behavior occurs for J_D-V_G curves with positive V_D (fig. S8E). Furthermore, the on-off ratio, which corresponds to the ratio between the highest and lowest currents in a J_D-V_G curve, decreases with increasing V_D. The highest on-off ratio of ~320 is achieved for PCP near V_D = 0 V. The on-off ratio decreases with increasing V_D, which can be attributed to electron transmission occurring over a wider bias window, with the conductance less sensitive to gating-induced movement of molecular energy levels. Similar transfer characteristics (Fig. 5B) and a V_D-dependent on-off ratio (fig. S8g) also appear for OPE3, although with a peak on-off ratio value of ~34, which is only 10% of the PCP value. These behaviors cannot be observed for the graphene device without SAMs (fig. S9, A to F), which is indicative of the unique field-effect behavior for the vertical molecular transistors. The V_D-dependent transfer characteristics for PCP and OPE3 were also investigated by theoretical simulations. From the theoretical transfer characteristics (I_D-V_G) for PCP (Fig. 5C) and OPE3 (Fig. 5D), as V_D changes from −0.1 to −0.8 V, it can be observed that, with increased negative V_D, on-off ratios decrease and the lowest current points shift to the negative

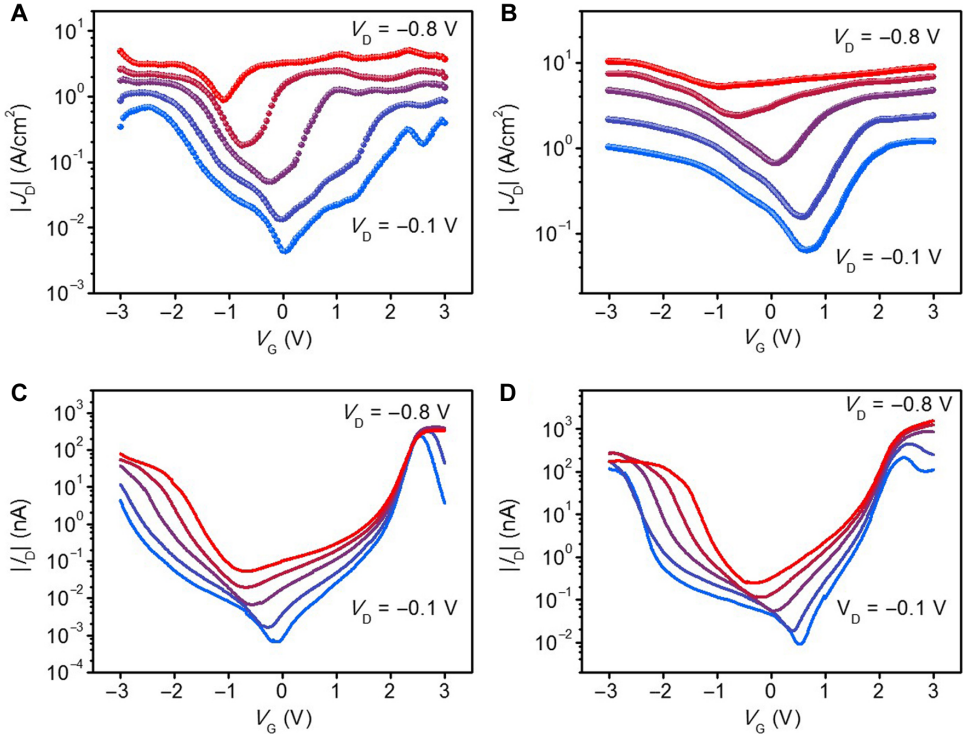

Fig. 5. Transfer characteristics for the vertical molecular transistors. (**A**) Experimental transfer characteristics for PCP. (**B**) Experimental transfer characteristics for OPE3. (**C**) Theoretical transfer characteristics for PCP. (**D**) Theoretical transfer characteristics for OPE3. V_D is varied from −0.1, −0.2, −0.4, −0.6, to −0.8 V in (A) to (D).

direction. In agreement with our measurements, the peak value of on-off ratio for PCP is about one order of magnitude higher than that of the OPE3 (fig. S8H).

CONCLUSION

In summary, we have demonstrated molecular transistors using vertical cross-plane graphene/SAM/gold heterostructures and ionic liquid gating. We show that charge transport across the vertical junction and transistor characteristics can be readily tailored by selecting molecules with or without destructive QI features (e.g., PCP- versus OPE3-based junctions). We show that a graphene/PCP-SAM/gold junction can show a significant current modulation by an ionic liquid gate, with a maximum on-off ratio of up to 330, which is about one order of magnitude higher than that for OPE3. This better gate behavior for PCP is a direct consequence of the zero-bias conductance suppression induced by destructive QI. The designed vertical molecular transistors with large on-off ratios could form the basic electronic building blocks for future electronics and may offer a robust platform for exploring gate-dependent quantum transport phenomena (*3*, *14*, *15*), especially when the ionic liquid gate is further replaced by a solid high-*k* gate (*27*). Furthermore, these QI-driven vertical molecular transistors, with sensitive gating applied outside of the top graphene electrode, can be further used for fabricating various functional devices, such as chemical and biological sensors (*28*, *29*).

MATERIALS AND METHODS

Device fabrication

A silicon wafer [single-side polished, N-type with arsenic dopant, (111) orientation, 0.001– to 0.004–ohm · cm resistivity, and 380-μm thickness coated by 300-nm thermally grown SiO_2] was cut into proper size and further cleaned for use. After a photolithographic process (a Karl Suss MA6 Contact Aligner, AZ 5214-E IR Photoresist, AZ Developer), a resist mask with a 80-μm hole was covered with silicon wafer. Next, a 300-nm SiO_2 layer in the patterned hole was selectively removed by buffered oxide etchant (BOE, 1:6 HF:NH_4F) for 5 min, which let the silicon surface exposed out. Then, the silicon wafer was annealed in air in a split tube furnace (Thermo Fisher Scientific Lindberg/Blue M) with a 1-inch quartz tube for 45 min at 960°C. During this annealing process, a 30-nm-thick layer of SiO_2 was thermally grown on the exposed silicon surface in the hole, which was confirmed by a film thickness measurement (SCI FilmTek 2000). After a second photolithographic process and an e-beam and thermal evaporation (CHA Mark 40 Evaporator), metal marks and gate electrode with Ti/Au (20/60 nm) were laid around the pretreated hole. With a poly(methyl methacrylate) (PMMA) layer [495, A8; 4000 revolutions per minute (rpm), 40 s; baked for 5 min at 150°C] spin coated on the sample, three square holes approaching 1.5 μm by 1.5 μm were fabricated by an e-beam lithography processes in the center of the 80-μm hole. Through the PMMA mask, a 30-nm SiO_2 layer in the patterned small holes was removed by BOE for 5 min, which let the conductive silicon surface exposed out. Immediately after the BOE etching, an ultraflat Ti/Au (5/23 nm) thin film was e-beam evaporated on the exposed silicon surface through the same mask with patterned small holes. After lifting off in acetone, the samples were stored in a vacuum desiccator for further use.

PCP and OPE3 were used as same with that in our previous work (*23*). Before molecule assembling, the samples with gold films were annealed at 250°C for 3 hours in a glove box [Glove Box Mikrouna, <1 parts per million (ppm) of O_2/H_2O]. For PCP and OPE3 assembling on the gold film on silicon wafers, 50 μM solutions of the SAc-protected wire in distilled toluene were prepared in the glove box (<1 ppm of O_2/H_2O). Then, the pretreated samples were immersed into 5 ml of corresponding solutions for at least 12 hours in the glove box. Two hours before taking the samples out for further fabrication, 0.09 ml of 0.05:20 DBU (1,8-diazabicyclo[5.4.0]undec-7-ene):distilled toluene solution was added into the reaction solution, and the reaction flask was shaken a little to help the mixing. After 2 hours, the samples were taken out from the vials and in turn washed with distilled toluene and ethanol three times by immersing the samples in fresh solvent. Last, the samples were blow dried with a N_2 gas stream.

A high-quality SLG was grown on 25-μm-thick copper films (Alfa Aesar), pretreated with glacial acetic acid, by using a low-pressure CVD method with optimal conditions (*30*). Then, a PMMA layer (495, A8; 2000 rpm, 30 s; baked for 2 min at 180°C) was spin coated on SLG/Cu. By using a wet etching technique, we etched the Cu layer with formation of a PMMA/SLG film. With aid of isopropanol, the PMMA/SLG film was transferred on samples with corresponding molecular SAMs. Next, with a photolithographic process and selective oxygen plasma etching (Tegal Plasmaline 515 System), graphene sheets were patterned to cover the 80-μm hole with SAMs at the center. After another photolithographic process, Ti/Au (20/60 nm) was thermally evaporated to make drain electrodes with connection to graphene sheets and source electrodes at the corner with connection to the back of the conductive silicon layer. Notably, before photoresist lift-off, a 30-nm Al_2O_3 layer was deposited by e-beam evaporation, and another 20-nm Al_2O_3 layer was deposited by atomic layer deposition (Cambridge Nanotech Inc., Savannah 100 and 200), which can passivate the surface of metal electrodes for reducing leakage current during ionic liquid gating. With another e-beam lithographic process and BOE etching, the covered Al_2O_3 layer on the source electrode at the corner was removed.

The compared graphene devices were fabricated by the same processes with the graphene layer directly deposited on top of the Ti/Au layer without SAMs. For the control 1-octadecanethiol (C18) devices, C18 SAMs were assembled by immersing the pretreated samples into 5 ml of 100 μM solutions of 1-octadecanethiol in anhydrous ethanol for 12 hours. Other fabrication processes were unchanged.

The fabricated devices were stored in a vacuum desiccator for further measurement. Before electrical measurements, a small drop of DEME-TFSI ionic liquid, where $DEME^+$ ions are the cations and $TFSI^-$ ions comprise the anions, was dropped on the device, covering the graphene-SAMs channel and the core part of gate electrode. Charge transport properties and ionic liquid gating performances of the devices were measured at room temperature (298 K) and 200 K by precision source/measure unit system (Keysight Agilent B2902A) and a Model TTPX cryogenic probe station (Lake Shore Cryotronics Inc.) with liquid nitrogen. The differential conductance data dJ/dV were obtained by numerical differentiation of the corresponding J versus V data.

Device characterization

Bruker Dimension FastScan Scanning Probe Microscope (SPM) was used for AFM measurements of the prepared samples with a tapping mode. The measured AFM images were further analyzed by a Nanoscope analysis software. Kratos Axis Ultra XPS system (AlKα radiation; power, ≤180 W) was used for obtaining high-resolution XPS (HR-XPS) data of the samples.

Raman measurements were carried out on a LabRAM HR Evolution Raman spectrometer (Horiba Scientific) with an excitation wavelength

of 632.8 nm. A gold film with a thickness of 8 nm was used for surface-enhanced Raman spectroscopy of SAM samples (*31*).

Computational details

The ground-state Hamiltonian and optimized geometry of each molecule was obtained using the density functional theory code SIESTA (Spanish Initiative for Electronic Simulations with Thousands of Atoms) (*32*). The local density approximation exchange correlation functional was used along with double zeta-polarized (DZP) basis sets and norm-conserving pseudo-potentials. The real space grid is defined by a plane-wave cutoff of 185 rydberg. The geometry optimization was carried out to a force tolerance of 0.01 eV/Å. This process was repeated for a unit cell with the molecule between gold and graphene electrodes, where the optimized distance between graphene and the thiol anchor group was found to be 2.9 Å.

Theoretical methods

To model the periodicity in the graphene and interaction between the molecules in the SAM, the unit cell was repeated using a Bravias lattice with 30 *k*-points in the *y* direction. This models an SAM where molecules are ~2 nm apart. The gold electrode is considered to be a nanowire and not periodic. A mean-field Hamiltonian and an overlap matrix were extracted from this converged calculation.

To model the source-drain and V_G in the experiment, we used a model where the gold lead is earthed, and therefore, the gold Fermi energy (E_F^{Gold}) is not affected by the source-drain or gate voltage. However, the Fermi energy of graphene is a function of the source-drain and gate voltages via the equation

$$E_F^{Gr}(V_D, V_G) = E_F^{Gold} - \alpha V_D - \beta V_G \quad (1)$$

where V_D and V_G are the source-drain and gate voltages, and α and β are the experimental lever arms, which could vary in each experiment. Similarly, applying a V_G can move the energy levels of the molecule up and down in energy (Eqs. 2 and 3)

$$\varepsilon^{HOMO}(V_G) = \varepsilon_m^{HOMO} - \gamma_G V_G \quad (2)$$

$$\varepsilon^{LUMO}(V_G) = \varepsilon_m^{LUMO} - \gamma_G V_G \quad (3)$$

The value for current is given by Eq. 4

$$I(V_D, V_G) = \frac{2e}{h}\int_{E_F^{Gold}}^{E_F^{Gr}(V_D,V_G)} T(E, V_D, V_G)dE \quad (4)$$

where $T(E, V_D, V_G)$, is the transmission coefficient from lead 1 to lead 3 calculated using quantum transport code the GOLLUM (*26*). In what follows, $\gamma_G = 1$. When comparing theory with experiment, e.g., in Fig. 2, a lever arm of $\alpha = 0.44$ was used.

SUPPLEMENTARY MATERIALS

Supplementary material for this article is available at http://advances.sciencemag.org/cgi/content/full/4/10/eaat8237/DC1

REFERENCES AND NOTES

1. S. V. Aradhya, L. Venkataraman, Single-molecule junctions beyond electronic transport. *Nat. Nanotechnol.* **8**, 399–410 (2013).
2. D. Xiang, X. Wang, C. Jia, T. Lee, X. Guo, Molecular-scale electronics: From concept to function. *Chem. Rev.* **116**, 4318–4440 (2016).
3. S. Thiele, F. Balestro, R. Ballou, S. Klyatskaya, M. Ruben, W. Wernsdorfer, Electrically driven nuclear spin resonance in single-molecule magnets. *Science* **344**, 1135–1138 (2014).
4. W. Du, T. Wang, H.-S. Chu, L. Wu, R. Liu, S. Sun, W. K. Phua, L. Wang, N. Tomczak, C. A. Nijhuis, On-chip molecular electronic plasmon sources based on self-assembled monolayer tunnel junctions. *Nat. Photonics* **10**, 274–280 (2016).
5. P. Reddy, S.-Y. Jang, R. A. Segalman, A. Majumdar, Thermoelectricity in molecular junctions. *Science* **315**, 1568–1571 (2007).
6. C. J. Lambert, Basic concepts of quantum interference and electron transport in single-molecule electronics. *Chem. Soc. Rev.* **44**, 875–888 (2015).
7. C. M. Guédon, H. Valkenier, T. Markussen, K. S. Thygesen, J. C. Hummelen, S. J. Van Der Molen, Observation of quantum interference in molecular charge transport. *Nat. Nanotechnol.* **7**, 305–309 (2012).
8. T. A. Su, M. Neupane, M. L. Steigerwald, L. Venkataraman, C. Nuckolls, Chemical principles of single-molecule electronics. *Nat. Rev. Mater.* **1**, 16002 (2016).
9. C. Jia, A. Migliore, N. Xin, S. Huang, J. Wang, Q. Yang, S. Wang, H. Chen, D. Wang, B. Feng, Z. Liu, G. Zhang, D.-H Qu, H. Tian, M. A. Ratner, H. Xu, A. Nitzan, X. Guo, Covalently bonded single-molecule junctions with stable and reversible photoswitched conductivity. *Science* **352**, 1443–1445 (2016).
10. N. Xin, J. Wang, C. Jia, Z. Liu, X. Zhang, C. Yu, M. Li, S. Wang, Y. Gong, H. Sun, G. Zhang, J. Liao, D. Zhang, X. Guo, Stereoelectronic effect-induced conductance switching in aromatic chain single-molecule junctions. *Nano Lett.* **17**, 856–861 (2017).
11. X. Yin, Y. Zang, L. Zhu, J. Z. Low, Z.-F. Liu, J. Cui, J. B. Neaton, L. Venkataraman, L. M. Campos, A reversible single-molecule switch based on activated antiaromaticity. *Sci. Adv.* **3**, eaao2615 (2017).
12. B. Capozzi, J. Xia, O. Adak, E. J. Dell, Z.-F. Liu, J. C. Taylor, J. B. Neaton, L. M. Campos, L. Venkataraman, Single-molecule diodes with high rectification ratios through environmental control. *Nat. Nanotechnol.* **10**, 522–527 (2015).
13. X. Chen, M. Roemer, L. Yuan, W. Du, D. Thompson, E. del Barco, C. A. Nijhuis, Molecular diodes with rectification ratios exceeding 10^5 driven by electrostatic interactions. *Nat. Nanotechnol.* **12**, 797–803 (2017).
14. H. Song, Y. Kim, Y. H. Jang, H. Jeong, M. A. Reed, T. Lee, Observation of molecular orbital gating. *Nature* **462**, 1039–1043 (2009).
15. M. L. Perrin, E. Burzurí, H. S. van der Zant, Single-molecule transistors. *Chem. Soc. Rev.* **44**, 902–919 (2015).
16. K. Moth-Poulsen, T. Bjørnholm, Molecular electronics with single molecules in solid-state devices. *Nat. Nanotechnol.* **4**, 551–556 (2009).
17. C. Huang, A. V. Rudnev, W. Hong, T. Wandlowski, Break junction under electrochemical gating: Testbed for single-molecule electronics. *Chem. Soc. Rev.* **44**, 889–901 (2015).
18. Y. Liu, N. O. Weiss, X. Duan, H.-C. Cheng, Y. Huang, X. Duan, Van der Waals heterostructures and devices. *Nat. Rev. Mater.* **1**, 16042 (2016).
19. K. S. Novoselov, A. Mishchenko, A. Carvalho, A. H. Castro Neto, 2D materials and van der Waals heterostructures. *Science* **353**, aac9439 (2016).
20. J. C. Love, L. A. Estroff, J. K. Kriebel, R. G. Nuzzo, G. M. Whitesides, Self-assembled monolayers of thiolates on metals as a form of nanotechnology. *Chem. Rev.* **105**, 1103–1170 (2005).
21. K. Ueno, S. Nakamura, H. Shimotani, H. T. Yuan, N. Kimura, T. Nojima, H. Aoki, Y. Iwasa, M. Kawasaki, Discovery of superconductivity in $KTaO_3$ by electrostatic carrier doping. *Nat. Nanotechnol.* **6**, 408–412 (2011).
22. T. Tian, P. Rice, E. J. G. Santos, C.-J. Shih, Multiscale analysis for field-effect penetration through two-dimensional materials. *Nano Lett.* **16**, 5044–5052 (2016).

23. M. Carlotti, A. Kovalchuk, T. Wächter, X. Qiu, M. Zharnikov, R. C. Chiechi, Conformation-driven quantum interference effects mediated by through-space conjugation in self-assembled monolayers. *Nat. Commun.* **7**, 13904 (2016).
24. C. J. Lambert, S. X. Liu, A magic ratio rule for beginners: A chemist's guide to quantum interference in molecules. *Chemistry* **24**, 4193–4201 (2018).
25. T. Sato, G. Masuda, K. Takagi, Electrochemical properties of novel ionic liquids for electric double layer capacitor applications. *Electrochim. Acta* **49**, 3603–3611 (2004).
26. J. Ferrer, C. J. Lambert, V. M. García-Suárez, D. Z. Manrique, D. Visontai, L. Oroszlany, R. Rodríguez-Ferradás, I. Grace, S. W. D. Bailey, K. Gillemot, H. Sadeghi, L. A. Algharagholy, GOLLUM: A next-generation simulation tool for electron, thermal and spin transport. *New J. Phys.* **16**, 093029 (2014).
27. W. J. Yu, Z. Li, H. Zhou, Y. Chen, Y. Wang, Y. Huang, X. Duan, Vertically stacked multi-heterostructures of layered materials for logic transistors and complementary inverters. *Nat. Mater.* **12**, 246–252 (2013).
28. Y. Liu, X. Dong, P. Chen, Biological and chemical sensors based on graphene materials. *Chem. Soc. Rev.* **41**, 2283–2307 (2012).
29. C. Jia, Q. Wang, N. Xin, J. Zhou, Y. Gong, L. Li, Q. Sun, X. Guo, Logic control of interface-induced charge-trapping effect for ultrasensitive gas detection with all-mirror-image symmetry. *Adv. Mater. Technol.* **1**, 1600067 (2016).
30. C. Jia, J. Jiang, L. Gan, X. Guo, Direct optical characterization of graphene growth and domains on growth substrates. *Sci. Rep.* **2**, 707 (2012).
31. W. Xu, X. Ling, J. Xiao, M. S. Dresselhaus, J. Kong, H. Xu, Z. Liu, J. Zhang, Surface enhanced Raman spectroscopy on a flat graphene surface. *Proc. Natl. Acad. Sci. U.S.A.* **109**, 9281–9286 (2012).
32. J. M. Soler, E. Artacho, J. D. Gale, A. García, J. Junquera, P. Ordejón, D. Sánchez-Portal, The SIESTA method for ab initio order-*N* materials simulation. *J. Phys. Condens. Matter* **14**, 2745 (2002).
33. V. Kaliginedi, P. Moreno-Garcia, H. Valkenier, W. Hong, V. M. Garcia-Suarez, P. Buiter, J. L. H. Otten, J. C. Hummelen, C. J. Lambert, T. Wandlowski, Correlations between molecular structure and single-junction conductance: A case study with oligo(phenylene-ethynylene)-type wires. *J. Am. Chem. Soc.* **134**, 5262–5275 (2012).
34. N. Xin, C. Jia, J. Wang, S. Wang, M. Li, Y. Gong, G. Zhang, D. Zhu, X. Guo, Thermally activated tunneling transition in a photoswitchable single-molecule electrical junction. *J. Phys. Chem. Lett.* **8**, 2849–2854 (2017).

Acknowledgments

Funding: X.D. acknowledges financial support by ONR through grant number N00014-15-1-2368. Support from the UK EPSRC is acknowledged through grant nos. EP/N017188/1, EP/M014452/1, EP/P027156/1, and EP/N03337X/1. Support from the European Commission is provided by the FET Open project 767187–QuIET. R.C.C. and M.C. acknowledge financial support by European Research Council for the ERC starting grant 335473 (MOLECSYNCON). Y.H. acknowledges the financial support from NSF EFRI-1433541. We acknowledge the Nanoelectronics Research Facility at UCLA for technical support. **Author contributions:** X.D., C.J.L., and C.J. conceived and designed the experiments. C.J. performed most of the experiments including device fabrication, characterization, and data analysis. M.F. and I.M.G. performed the theoretical simulation and data analysis. M.C. and R.C.C. synthesized the molecules. Y.L., P.W., Z.F., M.D., C.W., and S.-J.L. assisted with device fabrication and characterization. Y.W. performed the AFM studies. Z.Z. performed the XPS studies. X.X. assisted with synthesis of the graphene samples. X.D., C.J.L., and Y.H. supervised the research. X.D., C.J.L., C.J., and M.F. co-wrote the paper. All authors discussed the results and commented on the manuscript. **Competing interests:** The authors declare that they have no competing interests. **Data and materials availability:** All data needed to evaluate the conclusions in the paper are present in the paper and/or the Supplementary Materials. Additional data related to this paper may be requested from the authors.

Submitted 9 April 2018
Accepted 4 September 2018
Published 12 October 2018
10.1126/sciadv.aat8237

Citation: C. Jia, M. Famili, M. Carlotti, Y. Liu, P. Wang, I. M. Grace, Z. Feng, Y. Wang, Z. Zhao, M. Ding, X. Xu, C. Wang, S.-J. Lee, Y. Huang, R. C. Chiechi, C. J. Lambert, X. Duan, Quantum interference mediated vertical molecular tunneling transistors. *Sci. Adv.* **4**, eaat8237 (2018).